November 10, 2020

Systematic study of nuclear effects in p+Al, p+Au, d+Au, and ^{3}He+Au collisions at $\sqrt{s_{_{NN}}}$ = 200 GeV using π^0 production at PHENIX

PHENIX Collaboration Author List (Brant will insert later)

PHENIX presents a systematic study of π^0 production from p+p, p+Al, p+Au, d+Au, and ^{3}He+Au collisions at $\sqrt{s} = 200$ GeV. For inelastic collisions, the nuclear modification factors, $R_{\rm xA}$, are consistent with unity for $p_{\rm T}$ above 8 GeV/c, but exhibit an enhancement in peripheral collisions and a suppression in central collisions. The enhancement and suppression characteristics are the same for all systems for the same centrality class. It is shown that for high $p_{\rm T}$ π^0 production the nucleons in the d and ^{3}He interact mostly independently with the Au nucleus and that the counter intuitive centrality dependence is likely due to a bias in the event selection. These observations disfavor models where parton energy loss has a significant contribution to nuclear modifications in small systems. Nuclear modifications at lower $p_{\rm T}$ resemble the Cronin effect – an increase of $R_{\rm xA}$ followed by a peak in central or inelastic collisions and a plateau in peripheral collisions. The peak has a characteristic ordering by system size as p+Au > d+Au > ^{3}He+Au > p+Al. This is the exact reverse order compared to what is predicted by current calculations based on initial state cold nuclear matter effects, suggesting the presence of other contributions to nuclear modifications, in particular at lower $p_{\rm T}$.

PACS numbers: 25.75.Dw

I. INTRODUCTION

Measurements of transverse momentum ($p_{\rm T}$) distributions of particles produced in hadronic collisions are commonly used to obtain information from these collisions. At the Relativistic Heavy Ion Collider (RHIC) at Brookhaven National Laboratory (BNL), studies of neutral pions have led to significant insights. The discovery of the suppression of high $p_{\rm T}$ neutral pions and charged hadrons [1] in Au+Au collisions was one of the first hints of parton energy loss in the strongly coupled Quark Gluon Plasma (QGP). The absence of any suppression in reference spectra from d+Au collisions [2], where the formation of a QGP was not expected, was critical to establish parton energy loss as the origin of the observed suppression in Au+Au collisions. The subsequent systematic studies of the suppression pattern of π^0 in Au+Au collisions at $\sqrt{s_{_{NN}}} = 200$ GeV relative to scaled p+p collisions at the same energy allowed for quantitative constraints to the medium transport coefficients [3].

In the study of heavy-ion collisions, data from p+p collisions are often thought to be a baseline for particle production in the absence of the QGP and data from collisions like p+A and d+Au have been used to benchmark so-called "cold nuclear matter" (CNM) effects. CNM effects capture a number of fundamentally different phenomena in the initial state prior to the collision, during the collision, and immediately following the collision. Generally speaking, initial state CNM effects are discussed as modifications to the parton distribution functions. These modifications include shadowing, anti-shadowing, the EMC effect, momentum smearing due to Fermi motion, and gluon saturation. In contrast, nuclear absorption would be considered a final state effect. Multiple scattering in the nucleus prior to or immediately following a hard scattering process falls in between.

Experimentally, evidence for CNM effects was first observed in the late 1970s when the ratio of the production cross sections of hadrons from p+A to p+p was found to vary with $p_{\rm T}$ [4, 5]. This variation has since been referred to as the "Cronin effect": a suppression at low $p_{\rm T}$ followed by an enhancement around 2–5 GeV/c that vanishes towards larger $p_{\rm T}$. Historically the Cronin effect was attributed to initial state hard scattering [6, 7], but this explanation remained unsatisfactory because it could not explain the much larger effect for protons compared to pions. Measurements of momentum spectra at RHIC in the early 2000s renewed interest in the Cronin effect. Various theoretical models were developed to explain the Cronin effect. Most models were based on hard and soft multiple scattering [8–12], but there were also some more unconventional approaches involving gluon saturation [13] or recombination effects [14]. To date, there is no full quantitative explanation of the Cronin effect.

It came as a surprise to find striking similarities of long range particle correlations observed in high multiplicity p+p and p+Pb collisions at the LHC [15–18] with those found in A+A collisions, since their presence in A+A collisions was typically associated with the collective expansion of a QGP. Similar correlations were found in d+Au collisions at RHIC [19]. These findings have profound consequences for the interpretation of p+A collisions as a benchmark for CNM effects and suggest that a QGP could be produced in these systems.

The PHENIX experiment has used the versatility of RHIC, which allows for collisions of light nuclei like p, d, and ^{3}He with larger nuclei, for systematic studies of particle correlations in small systems. In all systems studied, high multiplicity events show large azimuthal anisotropies, measured as v_2 and v_3, that can be related to the initial geometry of the collision system and the build-up of collective behavior of the produced particles [20–24], which would be indicative of QGP formation.

Results from long range correlations have prompted great interest in finding other evidence of the possible formation of a QGP in small systems, such as parton energy loss or thermal photon emission. In such studies, data sets are typically divided into "centrality classes" according to the particle multiplicity measured at forward rapidity on the side of the outgoing larger nucleus [25]. Indeed, in p+Pb collisions at the LHC [26] and d+Au collisions at RHIC [27], a suppression of the jet yield at high p_T was found for central collisions. However, the same analyses show a significant enhancement of the jet yield in peripheral collisions, putting in question if the observed suppression is due to energy loss [28] or whether there are other mechanisms at play, for example, x-dependent color fluctuation effects in protons [29, 30] or biases in the centrality selection due to energy conservation [31].

In this paper new data on the system size and centrality dependence of π^0 production is presented over a wide p_T range from 1 to 20 GeV/c from p+Al, p+Au, d+Au, and ^{3}He+Au collisions at $\sqrt{s_{_{NN}}} = 200\,\text{GeV}$ compared to p+p collisions at the same energy. The data samples were recorded by the PHENIX experiment during the 2008 (p+p 5.2 pb^{-1}, d+Au 80 nb^{-1}), 2014 (^{3}He+Au 24 nb^{-1}), and 2015 (p+p 60 pb^{-1}, p+Al 0.5 pb^{-1}, p+Au 0.2 pb^{-1}) RHIC runs. The new p+p data are combined with the published results from p+p data taking in 2005 [32].

II. EXPERIMENTAL SETUP

To reconstruct π^0, the Electromagnetic Calorimeter (EMCal) in the central arms of the PHENIX detector is used. The EMCal is segmented into eight sectors, four in the west and four in the east arm of the PHENIX experiment. The sectors in each arm cover 90 degrees in azimuth and ±0.35 in pseudo-rapidity. All sectors in the west and the two top sectors in the east arm are made of 2,592 lead-scintillator (PbSc) towers each. The other two sectors are composed of lead-glass (PbGl) crystals. For the analyses presented here only the PbSc sectors were used. At a distance of 5 meters from the interaction point the angular segmentation of the PbSc sectors is $\Delta\phi$ x $\Delta\eta \approx 0.01$ x 0.01. The energy resolution achieved is $\delta E/E \approx 2.1\% \oplus 8.3/\sqrt{E}\%$ and arrival times of clusters are recorded with a resolution of about 0.5 ns. Further details can be found in Ref. [33].

For event selection and for centrality characterization the beam-beam counters (BBCs) are used, one on the north and one on the south side of the central arms. For asymmetric collision systems, the smaller (projectile) nucleus travels towards the north side and the larger (target) nucleus travels towards the south side. Each BBC is comprised of 64 Čerenkov counter modules. The BBCs are located at ±1.44 m from the interaction point and cover a pseudo-rapidity range of $3.0 < |\eta| < 3.9$. The BBC modules have a timing resolution of about 0.1 ns.

While the EMCal and the BBC were identical for the 2008, 2014, and 2015 RHIC runs, there were new or modified detector components in the PHENIX setup each year. The most notable change was a silicon vertex tracker (VTX) installed in the central arm acceptance in 2011. Though the VTX and other new components are not used in this analysis, the effect on the material budget of the detector needs to be taken into account in the Monte Carlo simulation setup used to calculate efficiency and acceptance corrections for each data set.

III. DATA SAMPLES

Several data samples were taken with different trigger conditions for each of the collision systems. The Minimum-bias (MB) data samples require coincidental hits in each of the two BBCs. For the data recorded in 2014 and 2015 the event vertex was required to be within ±10 cm of the nominal z=0 position. For the data recorded in 2008 the requirement was ±30 cm.

The collected MB data samples correspond to about 88% of the inelastic cross section for d+Au and ^{3}He+Au, 84% for p+Au, 72% for p+Al, and 54% for p+p. The events that are not recorded by the MB trigger involve mostly single diffractive (SD) nucleon-nucleon collisions, which predominantly produce particles at forward or backward rapidity and thus do not lead to coincident hits in both BBCs. As the number of binary nucleon-nucleon collisions (N_{coll}) increases from p+p to ^{3}He+Au collisions, the effect of an individual SD nucleon-nucleon collision is averaged out and a larger fraction of the inelastic cross section is captured by the MB trigger.

All MB data samples in the analysis, except for the p+p samples, are subdivided into four centrality classes using the charge measured in the south BBC, which is the direction the heavier (target) nucleus travels. The selections are 0-20%, 20-40%, 40-60%, and the remainder of the MB sample (>60%). Here the percentage refers to the fraction of events relative to all inelastic collisions.

The high luminosity provided by RHIC enables the increase of the statistics at high p_T, beyond what the data acquisition bandwidth would allow using an MB trigger only, by taking data samples with a high energy threshold photon trigger (ERT). This trigger requires a minimum energy recorded in the EMCal trigger segments (4x4 towers grouped to trigger tiles). Three different energy thresholds were used for each collision system. The ERT trigger thresholds are summarized in Table I. No coincidence in the BBC was required. These samples are again divided into the same centrality classes as the MB sample.

During the ^{3}He+Au, p+Au, and p+Al data collection

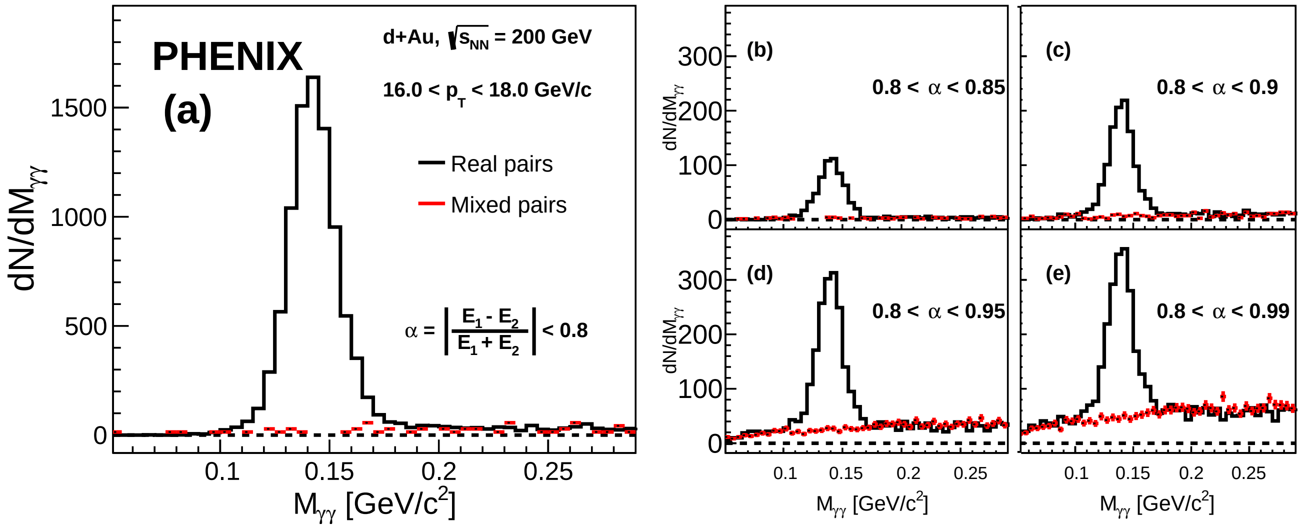

FIG. 1: Invariant mass example from d+Au collisions at $12 < p_T < 14\,\mathrm{GeV}/c$ (left). The mass peak is shown as the function of the asymmetry cut (α) on the two photons (right).

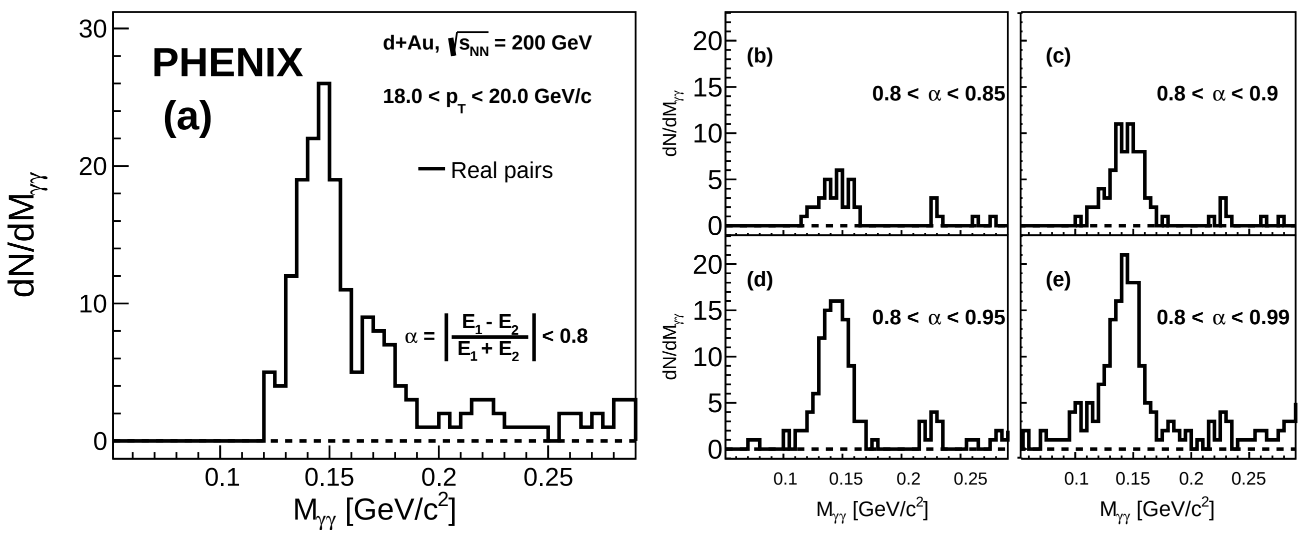

FIG. 2: Invariant mass example from d+Au collisions at $18 < p_T < 20\,\mathrm{GeV}/c$ (left). The mass peak is shown as the function of the asymmetry cut (α) on the two photons (right).

TABLE I: ERT trigger thresholds for each collision system.

		p+p	p+Al	p+Au	d+Au	^{3}He+Au
[GeV]	ERTA	2.1	2.8	2.8	2.8	3.5
	ERTB	2.8	3.5	3.5	3.5	4.0
	ERTC	1.4	2.1	2.1	2.1	2.8

samples were also taken with a high multiplicity trigger. This trigger required, in addition to the BBC coincidence, a larger minimum charge in the south BBC. In practice, the requirement was that a large number of modules should fire. The threshold was set to 25, 35, and 48 Čerenkov counter modules, for p+Al, p+Au, and ^{3}He+Au respectively. The thresholds were chosen such that the data samples approximately correspond to the top 5% most central collisions for each system.

IV. DATA ANALYSIS

Due to the high beam luminosity RHIC achieved since 2010, PHENIX has recorded an increased number of double interactions. The number of double interactions is largest for the p+p data taken in 2015 and is noticeable for p+Au and p+Al data taken the same year. The effect is negligible for the p+p, d+Au, and ^{3}He+Au data taken in 2008 and 2014, respectively. For the 2015 data, double interactions were reduced by making cuts on the time of flight measured for towers in the EMCal and the BBC Čerenkov modules. The cut on the EMCal requires the tower time to be within ± 5 ns of the expected arrival time. This eliminates towers that are from different beam crossings. The BBC timing cut is used to reduce pile-up collisions that happen during the same bunch crossing. Such events are identified by large deviations of the time measured for individual BBC Čerenkov modules from the event average. For data from 2014 and 2008 no cuts were applied. Any residual pileup events are accounted for in the systematic uncertainties.

The reconstruction of neutral pions is performed via the $\pi^0 \rightarrow \gamma\gamma$ decay channel. The methods used by PHENIX have been described extensively in Ref. [34] and will only be summarized in this paper. As a first step, neighbouring PbSc towers with energy deposits above 0.015 GeV are grouped into clusters. All clusters within one sector that have an energy of at least 0.3 GeV are combined into pairs. A minimum distance of 8 cm between the two cluster centers is required, corresponding to about 1.5 tower separation between clusters. For each remaining pair, the invariant mass ($M_{\gamma\gamma}$) and transverse momentum (p_{T}) is calculated. Invariant mass distributions are generated in bins of p_{T} and collision centrality. All mass distributions show a clear peak at the π^0 mass and a combinatorial background that is largest at events with low p_{T} and in central collisions.

To extract the π^0 yield, the background in the π^0 peak region needs to be subtracted. For p_{T} below 12 GeV/c an asymmetry cut of $\alpha < 0.8$ is applied to reduce the combinatorial background. Here the asymmetry is defined as $\alpha = \left|\frac{(E_1 - E_2)}{(E_1 + E_2)}\right|$, where E_1 and E_2 are the energy of the two photon clusters. For p_{T} above 12 GeV/c the cut is relaxed to $\alpha < 0.95$ as discussed below.

The bulk of the background is estimated and subtracted by an event mixing technique that combines clusters from different events with similar vertex position (z_{vtx}) and centrality. The shape of the mass distributions obtained from mixed events does not perfectly describe the combinatorial background in data. The mismatch results from correlated clusters in the event that are not accounted for in the mixed event technique.

For the MB samples, the mismatch is small and a two-step procedure is used for the subtraction. First, the mass distribution from mixed events is normalized in the mass region below and above the π^0 peak, $0.05 < M_{\gamma\gamma} < 0.1$ GeV/c and $0.2 < M_{\gamma\gamma} < 0.4$ GeV/c, respectively. After subtracting the normalized distributions from all bins, a residual background remains. This is approximated by a first-order polynomial that is fitted to the same mass regions around the π^0 peak and then also subtracted.

For the ERT data samples, the shape difference is more significant and thus a different approach is used. Instead of normalizing the mixed event distribution with a constant, the ratio of data/mixed events is fit with a second-order polynomial in the window around the π^0 peak. This function is then used to normalize the mixed event distributions bin-by-bin. No residual background subtraction is needed in this case.

At very high-p_{T}, typically > 15 GeV/c, the combinatorial background is so small that neither normalization strategy for the mixed events gives stable results. Instead, the average count per mass bin, determined in the region below and above the π^0 peak, is subtracted. Yields of π^0 are calculated from the mass spectra after completed background subtraction by counting the entries within 2σ of the peak, where the σ is set by fitting the counts in the π^0 region to a Gaussian.

Above 12 GeV/c, the two photon clusters from the π^0 begin to overlap more and more and frequently merge into a single cluster. The asymmetry cut at $\alpha < 0.8$, which was used to reduce the combinatorial background, starts to limit the π^0 reconstruction efficiency and with it the effective p_{T} reach of the measurement. Because the combinatorial background is rather small at high p_{T}, the asymmetry cut can be relaxed in order to increase the reconstruction efficiency. Figure 1 and Figure 2 shows mass distributions from d+Au collisions in the 12 to 14 GeV/c and 18 to 20 GeV/c p_{T} bins with different asymmetry cuts. The additional statistics recovered by extending the asymmetry cut is clearly visible. In particular, in the higher p_{T} bin, increasing the cut from $\alpha < 0.8$ to < 0.95 effectively doubles the statistics. Since it is also evident that the background increases, the looser cut is only used above $p_{\mathrm{T}} > 12$ GeV/c. The background subtraction and π^0 yield calculation follow the same steps as outlined above for lower p_{T}. The background estimate from event mixing is also shown on Figure 1. For the case of Figure 2, the background is estimated from the average bin content around the π^0 peak.

At this stage of the analysis, raw π^0 yields are available for all data samples in different bins of p_{T} and centrality. In the next step the raw yields from the MB and ERT trigger samples are combined for a given collision system and centrality. First, the ERT trigger samples are corrected for the trigger efficiency, which has a smooth turn around the trigger energy threshold and plateaus near 100% at higher p_{T}. A data driven method is used that compares the ERTC to the MB sample and the ERTA/ERTB to the ERTC sample to establish the turn on curve of the different trigger thresholds. The corrected spectra agree very well in the range where the trigger efficiency is larger than 30%.

In order to assure the largest statistical accuracy in each p_{T} bin, the MB triggered events are used in the low-p_{T} region, the ERTC trigger in the mid-p_{T} region, and the ERTB trigger at high-p_{T}. These transitions happen at different p_{T} thresholds for different collision systems. The p_{T} thresholds are set near the point where the trigger efficiency reaches its plateau value, typically close to twice the trigger threshold shown in Table I. The ERTA

TABLE II: Summary of the $N_{\rm coll}$, $N_{\rm part}$, $N_{\rm proj}$, f_{bias} calculated using a Glauber Monte Carlo simulation. The ratio $N_{\rm coll}/N_{\rm proj}$ is also quoted for d and ^{3}He projectiles, since some systematic uncertainties cancel in this ratio. The last column is the measured charged particle multiplicity ($dN_{ch}/d\eta$) in the mid-rapidity region.

system	centrality	$N_{\rm coll}$	$N_{\rm part}$	$N_{\rm proj}$	f_{bias}	$N_{\rm coll}/N_{\rm proj}$	$dN_{ch}/d\eta$
p+p		1	2	1	0.73±0.07	-	2.38±0.09
p+Al	0-5%	4.1±0.3	4.5±0.3	1	0.81±0.01	-	5.5±0.8
	0-20%	3.4±0.3	4.4±0.3	1	0.81±0.01	-	5.13±0.73
	20-40%	2.3±0.1	3.3±0.1	1	0.90±0.02	-	4.0±0.6
	40-60%	1.8±0.1	2.8±0.2	1	0.99±0.03	-	3.32±0.3
	60-72%	1.3±0.1	2.3±0.2	1	1.15±0.06	-	2.7±0.1
	0-100%	2.1±0.1	3.1±0.1	1	0.8±0.02	-	3.96±0.54
p+Au	0-5%	9.7±0.6	10.7±0.6	1	0.86±0.01	-	12.3±1.7
	0-20%	8.2±0.5	9.2±0.5	1	0.90±0.01	-	10.38±1.45
	20-40%	6.1±0.4	7.1±0.4	1	0.98±0.01	-	7.7±1.1
	40-60%	4.4±0.3	5.4±0.3	1	1.02±0.01	-	5.7±0.8
	60-84%	2.6±0.2	3.6±0.2	1	1.00±0.06	-	3.5±0.5
	0-100%	4.7±0.3	5.7±0.3	1	0.858±0.014	-	6.66±0.94
d+Au	0-5%	18.1±1.2	17.8±1.2	1.97±0.02	0.91±0.01	8.98±0.59	18.9±1.4
	0-20%	15.1±1.	15.2±0.6	1.95±0.01	0.94±0.01	7.46±0.50	16.38±1.2
	20-40%	10.2±0.7	11.1±0.6	1.84±0.01	1.00±0.01	5.71±0.39	12.2±0.9
	40-60%	6.6±0.4	7.8±0.4	1.65±0.02	1.03±0.02	4.16±0.28	8.7±0.6
	60-88%	3.2±0.2	4.3±0.2	1.36±0.02	1.03±0.06	2.27±0.15	4.1±0.3
	0-100%	7.6±0.4	8.6±0.4	1.62±0.01	0.889±0.003	4.35±0.24	9.5±1.0
^{3}He+Au	0-5%	26.8±2.0	25.0±1.6	2.99±0.01	0.92±0.01	8.72±0.64	23.6±2.6
	0-20%	22.3±1.7	21.8±1.3	2.95±0.01	0.95±0.01	7.30±0.52	21.28± 2.3
	20-40%	14.8±1.1	15.4±0.9	2.75±0.03	1.01±0.01	5.41±0.37	16.1±1.8
	40-60%	8.4±0.6	9.5±0.6	2.29±0.04	1.02±0.01	3.85±0.25	10.3±1.1
	60-88%	3.4±0.3	4.6±0.3	1.56±0.05	1.03±1.05	2.05±0.12	4.4±0.5
	0-100%	10.4±0.7	11.4±0.5	2.22±0.02	0.89±0.01	4.13±0.24	12.24±1.35

triggered samples are used to crosscheck the results.

Next, the raw $p_{\rm T}$ spectra need to be corrected for distortions due to the finite detector acceptance, inefficiencies in the π^0 reconstruction, limited energy resolution, etc.. These are determined simultaneously as one single correction as a function of $p_{\rm T}$ using a full Monte Carlo simulation of the PHENIX detector setup. They are commonly referred to as acceptance-efficiency corrections. For each running period, a separate simulation setup is used that describes the PHENIX detector configuration specific to that period. Samples of single π^0 are simulated with a flat $p_{\rm T}$ distribution from 0 to 30 GeV/c, full azimuthal coverage, and in one unit of rapidity at mid-rapidity. These π^0 are tracked through the full simulation of the PHENIX detector setup for the different running periods. The resulting simulated detector responses are embedded into real data from the same running period and reconstructed using the same analysis methods applied to the data. Great care was taken to tune the simulation so that π^0 peak positions and widths reconstructed from the simulation match the experimental data. Each reconstructed π^0 is weighted with a realistic "trial" production probability for the $p_{\rm T}$ of the input π^0. Since the true production probability is unknown, the weighting needs to be iterated. For this the "trial" probability is multiplied by the ratio of the measured raw π^0 distribution over the reconstructed π^0 distribution from the simulation. The modified "trial" probability is then used as the new weight. The process is iterated until convergence, which typically requires only a few steps. The final acceptance-efficiency corrections are calculated as the ratio of the probability to reconstruct a π^0 at a given $p_{\rm T}$ over the production probability at that $p_{\rm T}$ in one unit of pseudo-rapidity at midrapidity and 2π in azimuth. The acceptance-efficiency corrections are determined separately for each centrality selection in order to account for any multiplicity dependent effects.

Additionally, each collision system and each centrality selection for a given collision system must be corrected for the bias towards higher event multiplicity and hence higher centrality for non-diffractive nucleon-nucleon collisions compared to diffractive collision events with the same impact parameter (see [25] for full details). The bias factor f_{bias}, which is used to scale the $p_{\rm T}$ spectra, is calculated using a Glauber Model Monte Carlo calculation [35] in conjunction with the assumption of a negative-binomial multiplicity distribution of particles produced in individual nucleon-nucleon collisions. The same Glauber calculation is used to characterize each centrality class by the number of binary nucleon-nucleon collisions N_{coll}, number of nucleon participants N_{part}, and other relevant properties related to the collision geometry like N_{proj}, the number of participants in the projectile nucleus. For MB collisions, the f_{bias} also includes the extrapolation from the recorded cross section to the full inelastic cross section (0-100% centrality). The N_{coll}, N_{part}, N_{proj}, and f_{bias} values are given in Table II.

V. SYSTEMATIC UNCERTAINTY

There are many sources of systematic uncertainty that need to be evaluated. They are separated into two groups: (i) uncertainty on the event characterization, and (ii) on the π^0 yield extraction.

The event characterization is done using Glauber model simulations and the uncertainties were determined by varying the input to the Glauber model and various assumptions used in [25]. The results are included in Table II. All quantities extracted from the Glauber model simulation are correlated, which leads to a partial cancellation of the uncertainties. This was taken into account.

The uncertainties on the π^0 invariant yield are summarized in Table III for the different running periods. The total uncertainty on the π^0 invariant yield varies between 8-10% for p_{T} below 8 GeV/c and increases to nearly 15% at 20 GeV/c. They have little dependence on collision systems or centrality selection. The uncertainties on the π^0 invariant yield were obtained with similar methods for all data sets. They are highly correlated within a running period and somewhat correlated between running periods. These correlations have been taken into account when combining data sets or calculating ratios of data sets. The remainder of this section provides more details on the evaluation of the systematic uncertainties on the π^0 yield determination, which is split into the extraction of the raw π^0 yield and the corrections that need to be applied to it.

A. Raw π^0 Yield Extraction

The raw π^0 yield is extracted from an invariant mass $M_{\gamma\gamma}$ distribution, which involves the subtraction of a background distribution below a π^0 peak. Except for very high p_{T} this is done using the mixed event technique. This subtraction is typically accurate to better than 4%. In general, the uncertainties on the background subtraction are determined by changing the assumption on the shape of the background and how it is normalized. Many different strategies can be used, as they all give similar results. Here, one example is given, the strategy that was used for the 2015 MB data sets, which were used to extract the π^0 yield at lower p_{T} values for p+Au, p+Al, and p+p. The normalization of the mixed event background is determined in different ranges below and above the π^0 peak. For any normalization, after the mixed event subtraction there is a residual background, which is then fitted. For each normalization the fit range is varied to extract the residual background via a first-order polynomial. Then in each case the window for the π^0 yield extraction is varied from 1 to 3 sigma around the π^0 peak. The variation of the resulting π^0 yields, after correcting for the different σ ranges, is used to estimate the systematic uncertainty.

The accuracy with which the π^0 yield can be extracted depends on the amount of background. In general, the smaller the particle multiplicity in the event and/or the larger the π^0 p_{T}, the smaller the background. However, the accuracy with which the background can be determined for a particular p_{T} and centrality bin is driven by the available statistics. Since the π^0 p_{T} spectra is a result of combining MB and various ERT triggered data sets, the p_{T} dependence of the π^0 extraction uncertainty may sometimes show counter-intuitive decreasing uncertainty with increasing p_{T}.

B. Corrections of the Raw Yield

The acceptance-efficiency correction accounts for all distortions to the π^0 spectra that can be evaluated with the detailed simulation of π^0 measurements in the PHENIX experiment. The accuracy of the simulation determines the size of systematic uncertainties. Thus, great care is taken to assure that the output of the simulation agrees with the data.

These distortions include, besides the actual corrections for detector acceptance and π^0 reconstruction, the one for the energy scale and resolution, merging of clusters, and losses due to photon conversions. While the corrections were determined simultaneously, possible uncertainties are studied separately. In Table III these are identified as "Acceptance/Efficiency", "Energy Scale", "Cluster Merging", and "Conversion Loss", respectively.

The energy scale and resolution was tuned by matching the π^0 peak position and width in simulation and data, as function of p_{T}, to a better than 0.5–1% agreement, depending on the data set. The uncertainty is then determined by varying the energy scale and resolution within the achieved accuracy. The π^0 yields are consistent within 4-5% at 2 GeV/c and up to 7-9% at 20 GeV/c.

To study the accuracy of the reconstruction efficiency correction, cuts applied in the π^0 reconstruction were varied and the analysis was repeated. The changes in the π^0 yield were used to set the systematic uncertainties. They are typically smaller than 4%, but may be limited by statistical uncertainties. The uncertainty on the acceptance was determined from the precision of the survey of the EMCal. It is negligible compared to the uncertainties on the reconstruction efficiency.

TABLE III: Summary of systematic uncertainties on the π^0 invariant yields from different running periods.

Systematic uncer.	2015 p+Au, p+Al, p+p			2014 ^{3}He+Au			2008 d+Au, p+p		
p_T [GeV/c]	2	8	20	2	8	20	2	8	20
Peak Extraction	4.4%	3.4%	1%	2.7%	4.1%	2%	4.8%	2.9%	1.5%
Energy Scale	3.8%	6.5%	7.1%	3.0%	5.2%	5.7%	4.6%	7.9%	8.7%
Acceptance-Efficiency	3%	2.5%	1%	4	4%	4%	3%	2.5%	1%
Cluster Merging	0%	0%	9.0%	0%	0%	12%	0%	0%	10%
Conversion Loss	5%	5%	5%	5%	5%	5%	2.5%	2.5%	2.5%
Double Interactions	4%	3%	4%	<1%	<1%	<1%	1%	2.5%	4%
Off Vertex Decays	3%	3%	3%	3%	3%	3%	3%	3%	3%
Total	9.6%	10.1%	13.0%	8.3%	9.8%	14.1%	8.3%	10.0%	14.5%

The two decay photons from the decay of a high p_T π^0 are strongly boosted along the π^0 direction, the average opening angle becomes small, resulting in only a small separation between the impact points on the surface of the EMCal. At about 10 GeV/c, the two clusters start to merge. Initially, this happens only for very symmetric decays characterized by a small energy asymmetry (α). With increasing p_T, more and more clusters merge, leading to an increasing drop in reconstruction efficiency towards higher p_T. The accuracy with which the Monte Carlo simulation reproduces the cluster merging is verified by reconstructing π^0 from three exclusive asymmetry bins: 0–0.4, 0.4–0.8, and 0.8–0.95. After fully correcting the π^0 yields, the results are compared and the differences are used to estimate the systematic uncertainty. It reaches about 10% towards the end of the kinematic reach of the measurement.

Some photons convert into e^+e^- pairs before they reach the EMCal. If the radial location of the conversion point is close to the EMCal, outside the magnetic field, the e^+ and e^- will hit the EMCal in close proximity, resulting in one cluster with the full energy of the converted photon. In that case, it is likely that the π^0 is reconstructed. However, if the conversion point is closer to the vertex, and in the magnetic field, the π^0 will not be reconstructed, since the electron tracks bend in opposite direction, depositing their energy in two separate clusters. Prior to 2010, before the VTX was installed, about 81% of the π^0 were reconstructed. Due to the additional material of the VTX detector close to the vertex, this number drops to 61% after 2010. The accuracy with which the loss can be determined depends solely on the accuracy with which the material budget is known and implemented in the Monte Carlo simulation. The resulting uncertainties on the π^0 yield are 2.5% and 5%, before and after installation of the VTX. There is no significant momentum dependence.

All data sets from 2015 (p+p, p+Al, and p+Au) were taken at high beam luminosity, resulting in a significant number of recorded double interactions. These were actively identified and removed by timing cuts on the EMCal and BBC. The effect of any remnant double interaction was estimated by splitting the data samples into subsets taken at higher, medium, and lower luminosity. The analysis was repeated for each sample, and the π^0 yields were found to be consistent within 3-4%. This difference was assigned as systematic uncertainty. For the 2008 data sets (p+p and d+Au), only the EMCal timing cuts were applied to remove pileup events. Here, the possible contamination was estimated by the number of π^0 for which at least one cluster had a time off by >5 ns. The contribution was 1% at high p_T and about 4% at lower p_T. For the 2014 ^{3}He+Au data no sizable effect was found.

Some reconstructed π^0 originate from weak decays that occur at a significant distance from the interaction point, so called "off vertex π^0 ". The main source of such π^0 are decays of $K_s \rightarrow \pi^0\pi^0$. This source was extensively studied and found to drop from approximately 5% at 1 GeV/c to 3% at 2 GeV/c from where on it remains approximately constant. The small p_T dependence of this contribution is due to the two arm acceptance of the PHENIX detector, where the high-p_T decay products are more likely to be inside the acceptance. This contribution was not subtracted from the π^0 spectra and a 3% systematic uncertainty is assigned to it.

Finally, the uncertainty of the the normalization of the data taken with the ERT trigger to the MB data is examined. This uncertainty is smaller than 1% and not listed in Table III.

VI. RESULTS AND DISCUSSION

A. The p+p reference

PHENIX has previously published the π^0 p_T spectrum from p+p collisions at $\sqrt{s} = 200$ GeV [32] based on data taken in 2005 corresponding to 3.4 pb^{-1}. In 2008 and 2015 RHIC provided further p+p collisions, increasing the integrated luminosity by 5.2 pb^{-1} and 60 pb^{-1} respectively.

With the increased statistics, the precision of the measurement was improved and extended to higher p_T. Since the detector configurations and the ERT trigger settings were different for the 2008 and 2015 data sets, the π^0 spectra were measured separately. The results were combined with those from 2005.

The new and published measurements were made with the PHENIX EMCal using the same analysis strategy, thus the π^0 yield determinations have largely, but not completely, correlated systematic uncertainties. To combine the three data sets, the correlations between individual systematic uncertainties were carefully studied and accounted for using the BLUE method [36]. In addition to the uncertainties due to the π^0 reconstruction, there is an overall normalization uncertainty of 9.7% [32] that accounts for the limited accuracy with which the p+p MB trigger efficiency (see Table II) is known. This uncertainty is common to all p+p measurements.

In Figure 3, the combined π^0 p_T spectrum from p+p collisions (2005, 2008, 2015) is compared to the earlier published result. The combined result is in excellent agreement with data taken in 2005, but has significantly improved statistics and extends the p_T range up to 25 GeV/c. The systematic uncertainties are slightly reduced with respect to those of the 2005 data alone.

Also shown in Figure 3 are next-to-leading order pQCD calculations [37] with two different fragmentation functions (BKK and KKP FF) and for three different scales $\mu = p_\mathrm{T}/2$, p_T, and $2p_\mathrm{T}$. Within the assumed range of scales both fragmentation functions are consistent with the data. BBK would require a scale of $\mu = p_\mathrm{T}$, while KKP describes the data best at a slightly larger scale.

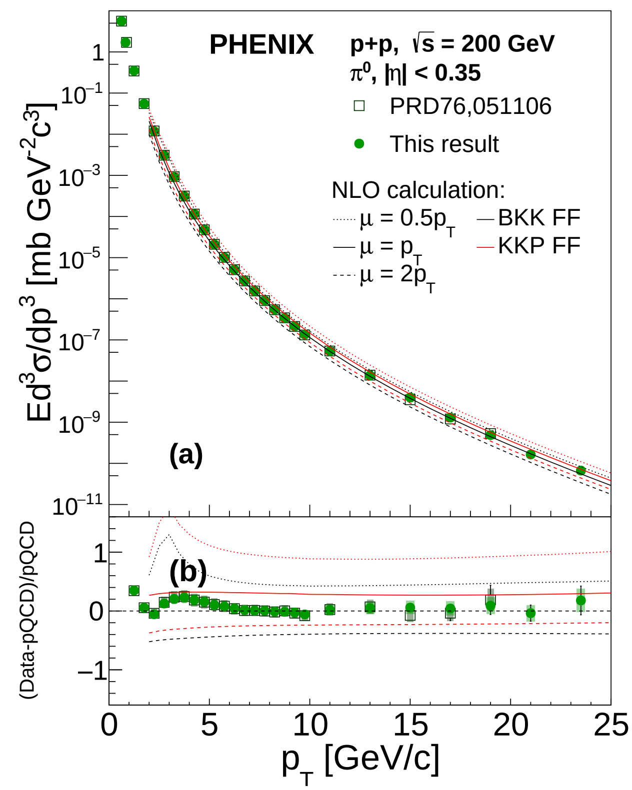

FIG. 3: Differential cross section of π^0 in p+p collisions at $\sqrt{s} = 200$ GeV. The data are compared with a pQCD calculation. The lower panel shows the ratio of the data points to the NLO calculation with BBK and a scale of $\mu = p_\mathrm{T}$.

B. Small system p_T spectra and nuclear modification factor

1. p_T spectra

Figure 4 presents π^0 p_T spectra from p+Al, p+Au, d+Au, and ^{3}He+Au from left to right, respectively. The data are presented as the invariant π^0 yield per collision as a function of p_T. The 0–100% range corresponds to the full inelastic cross section. The other centrality ranges correspond to 0–5, 0–20, 20–40, 40–60, and above 60% measured percentile of the events selected according to the multiplicity measured in the BBC on the south side (heavy nucleus going side). Different centrality selections are scaled by factors 1/10 for visibility. The 0–5% centrality selection, which is available for ^{3}He+Au, p+Au, and p+Al collisions, was taken with a high multiplicity BBC trigger and has a p_T range limited to below 10 GeV/c.

2. Nuclear Modification Factor

For a quantitative comparison across systems and centrality selections the nuclear modification factor is used. It is defined as:

$$R_{xA} = \frac{dN_{xA}/dp_T \times \sigma_{pp}}{\langle N_{coll}\rangle \times d\sigma_{pp}/dp_T}, \quad (1)$$

where dN_{xB}/dp_T is the invariant yield per x+A collisions, $d\sigma_{pp}/dp_T$ is the invariant cross section in p+p collisions, $\sigma_{pp} = 42$mb is the inelastic p+p cross section, and N_coll is the average number of binary nucleon-nucleon collisions given in Table II. A nuclear modification factor of $R_{xA} = 1$ at high p_T indicates that π^0 production through hard scattering processes in $x + A$ collisions is well described by a superposition of p+p collisions.

3. R_xA for inelastic collisions

The nuclear modification factors for inclusive π^0 production from inelastic p+Al, p+Au, d+Au, and ^{3}He+Au collisions are shown in Figure 5. They are calculated using the p+p reference from the combined 2005, 2008, and 2015 data. The correlations of the systematic uncertainties on the π^0 reconstruction for different data sets are taken into account using the BLUE method [36]. The overall normalisation uncertainties on p+p and on N_coll

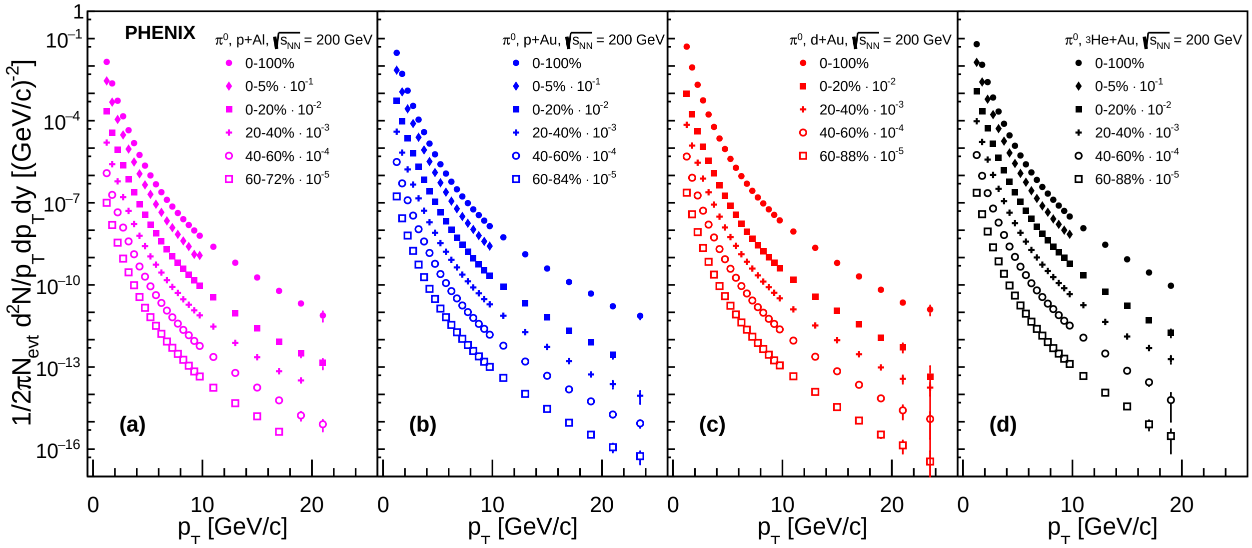

FIG. 4: Invariant yield of π^0 from (a) p+Al, (b) p+Au, (c) d+Au, and (d) ^{3}He+Au at $\sqrt{s_{NN}} = 200\,\text{GeV}$. For each collision system the yield is shown for the inelastic cross section and for different centrality selections 0-20%, 20-40%, 40-60%, and larger than 60%. For p+Al, p+Au, and ^{3}He+Au an additional 0–5% centrality selection is shown, which was recorded using a dedicated high multiplicity trigger.

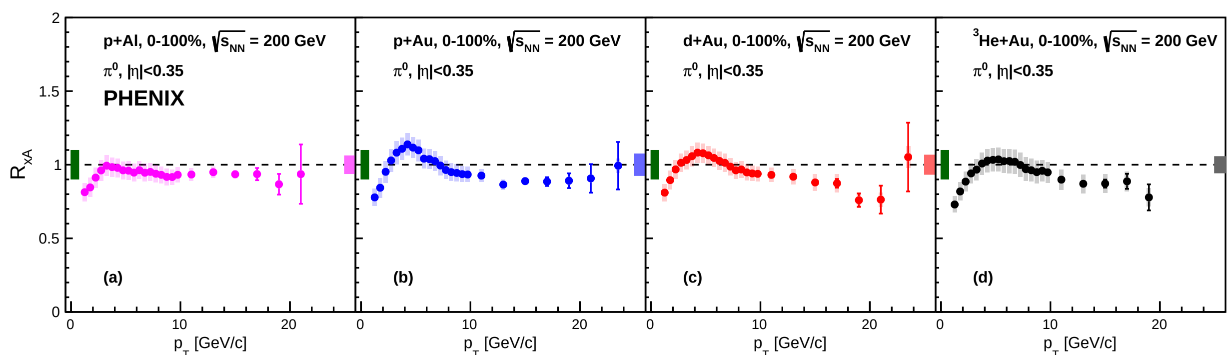

FIG. 5: Nuclear modification factors from inelastic p+Al, p+Au, d+Au, and ^{3}He+Au collisions at $\sqrt{s_{NN}} = 200\,\text{GeV}$. The error bars represent the statistical uncertainties, while the boxes represent the systematical uncertainties. The right boxes are the N_{coll} uncertainties from the Glauber model, while the left box represents the overall normalization uncertainty from p+p collisions.

are shown separately on the left and right on each panel, respectively.

Each data set exhibits the characteristic p_T dependence of the Cronin effect, an initial rise from below unity to a peak around p_T of $4\,\text{GeV}/c$, followed by a drop and a leveling off at high p_T. The constant value at high p_T is independent of the collision system at a value of $R_{xA} \sim 0.9$, which is consistent with unity within the systematic uncertainties on the scale and N_{coll}. The fact that R_{xA} at high p_T is consistent with unity and that there is no system size dependence suggest that there is little to no modification of the hard scattering component in small systems.

To investigate any possible system size dependence of the modification at lower p_T, the peak value in R_{xA} is determined as the ratio of integrated R_{xA} from 4 to $6\,\text{GeV}/c$ divided by the integral taken above $10\,\text{GeV}/c$. In these ratios the systematic uncertainties largely cancel. The peak values are 1.03 ± 0.018, 1.23 ± 0.012, 1.16 ± 0.009, and 1.16 ± 0.02 for p+Al, p+Au, d+Au, and ^{3}He+Au, respectively. The peak value is smallest in the smallest system and most pronounced in p+Au collisions.

The peak values are approximately the same as those calculated in fixed target p+A experiments [38] and as originally predicted for RHIC energies [8, 11, 12]. However, the systematic trend with system size does not follow the dependence observed at fixed target energies [5],

$$\frac{d\sigma_{xA}}{dp_T} = (xA)^{n(p_T)} \times \frac{d\sigma_{pp}}{dp_T}, \tag{2}$$

with a common exponent $n(p_T)$ for a given $\sqrt{s}$. Eq. 2 is re-written in terms of per event yield by using $\sigma_{xA} = xA\sigma_{pp}$, which is expected for particle production from hard scattering:

$$\frac{dN_{xA}}{dp_T} = (xA)^{n(p_T)-1} \times \frac{dN_{pp}}{dp_T}. \tag{3}$$

Comparing Eq. 3 and 1 gives a relation between $R_{\rm xA}$ and the exponent $n(p_T)$:

$$n(p_T) = 1 + \frac{\log(R_{xA})}{\log(xA)}. \tag{4}$$

The exponent $n(p_T)$ is calculated from the ratio of R_{pAu}/R_{pAl} and R_{HeAu}/R_{pAu}. All uncertainties on $N_{\rm coll}$ and the p+p data cancel for the nuclear modification factor ratios. The results are shown in Figure 6. The data show that there is no universal $n(p_T)$ at $\sqrt{s_{NN}} = 200\,{\rm GeV}$ below 8-10 GeV/c. At higher $p_{\rm T}$, the common $n(p_T)$ underlines the similarity of $R_{\rm xA}$ for all collision systems.

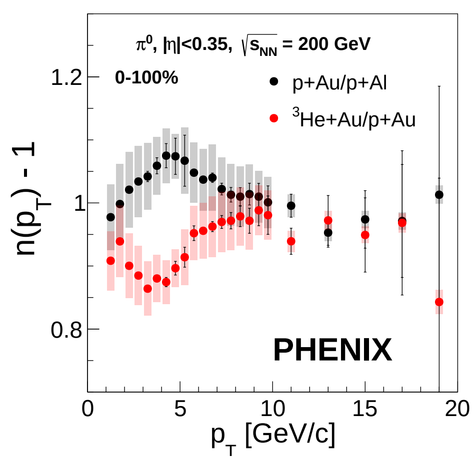

FIG. 6: Exponent according to the Eq. 4 as a function of transverse momenta extracted from p+Au/p+Al and ^{3}He+Au/p+Au collision systems. The uncertainties from the $N_{\rm coll}$ calculations and from the overall normalization of p+p cancel in these ratios.

4. $R_{\rm xA}$ *Centrality Dependence*

In Fig. 7, $R_{\rm xA}$ is shown for the different centrality selections from different collision systems. The scale uncertainty from the p+p reference and, to a large extent, the scale uncertainty due to $N_{\rm coll}$ only influences the scale of $R_{\rm xA}$, but not the relative differences between systems. The comparison reveals clear systematic trends of $R_{\rm xA}$ with centrality and system size.

For $p_{\rm T} > 8\,{\rm GeV}/c$, the $R_{\rm xA}$ values remain constant at similar values for the same centrality selection from different collision systems. However, the plateau value varies with centrality. $R_{\rm xA}$ is below unity in the more central collisions, consistent with unity in the 20–60% bin, and above or consistent with unity in the peripheral collisions. In the lower $p_{\rm T}$ range, the 0–5% and 0–20% selections exhibit a clear Cronin peak structure, similar to the inelastic collision case, but more pronounced. The peak is largest for p+Au. The height of the peak is system size dependent and decreases from p+Au, to d+Au, to ^{3}He+Au, i.e. with increasing size of the projectile nucleus. Similarly, the peak is smaller for p+Al than for p+Au, so it also seems to decrease with decreasing size of the target nucleus. In contrast, in peripheral collisions all systems follow a common trend. From central, to semi-central, to semi-peripheral collisions a gradual change is seen for each system, without apparent systematic trend across systems.

In order to better understand the trends, the average nuclear modification factor $\langle R_{\rm xA}\rangle$ is calculated for two distinct $p_{\rm T}$ regions, above 8 GeV/c to represent the high $p_{\rm T}$ region and from $4 < p_{\rm T} < 6$ GeV/c to capture the peak of $R_{\rm xA}$. These $\langle R_{\rm xA}\rangle$ are studied as function of variables characterizing centrality classes shown in Tab. II. Note that $N_{\rm coll}$ and $N_{\rm part}$ are highly correlated and follow a universal trend. $N_{\rm part} = N_{\rm coll} + 1$ up to an $N_{\rm coll}$ value of $\sim$14. For $N_{\rm coll} > 14$, $N_{\rm part}$ increases slightly slower with $N_{\rm coll}$. Consequently, common trends with one variable will also present themselves with respect to the other. The $\langle R_{\rm xA}\rangle$ is calculated as follows:

$$\langle R_{\rm xA}\rangle = \frac{\int \frac{dN_{AB}}{dp_T} dp_T}{N_{coll} \int \frac{dN_{pp}}{dp_T} dp_T} \tag{5}$$

Figure 8 shows $\langle R_{\rm xA}\rangle$ for the two $p_{\rm T}$ regions for all measured centrality selections from all collision systems. In the top panel $\langle R_{\rm xA}\rangle$ is plotted as function of $N_{\rm coll}$ and in the lower panels as function of $N_{\rm coll}$ per number of participating nucleons in the projectile $N_{\rm proj}$.

The $\langle R_{\rm xA}\rangle$ above 8 GeV/c exhibits no common trend as function of $N_{\rm coll}$ (panel b). $\langle R_{\rm xA}\rangle$ is below $N_{\rm coll}$ scaling for peripheral classes and above for central classes for all collision systems. The situation changes when looking at the $\langle R_{\rm xA}\rangle$ versus $N_{\rm coll}/N_{\rm proj}$ (panel d). The collision systems involving Au as a target nucleus (p+Au, d+Au, and ^{3}He+Au) follow a universal trend that is distinctly different from the one observed for p+Al. Modifications to binary scaling are approximately the same for p+Au and p+Al for the same centrality class, despite the difference in $N_{\rm coll}$ or $N_{\rm part}$. The same trends are observed for any choice of $p_{\rm T}$ threshold above 7 GeV/c up to 15 GeV/c, above which statistics become limiting. There

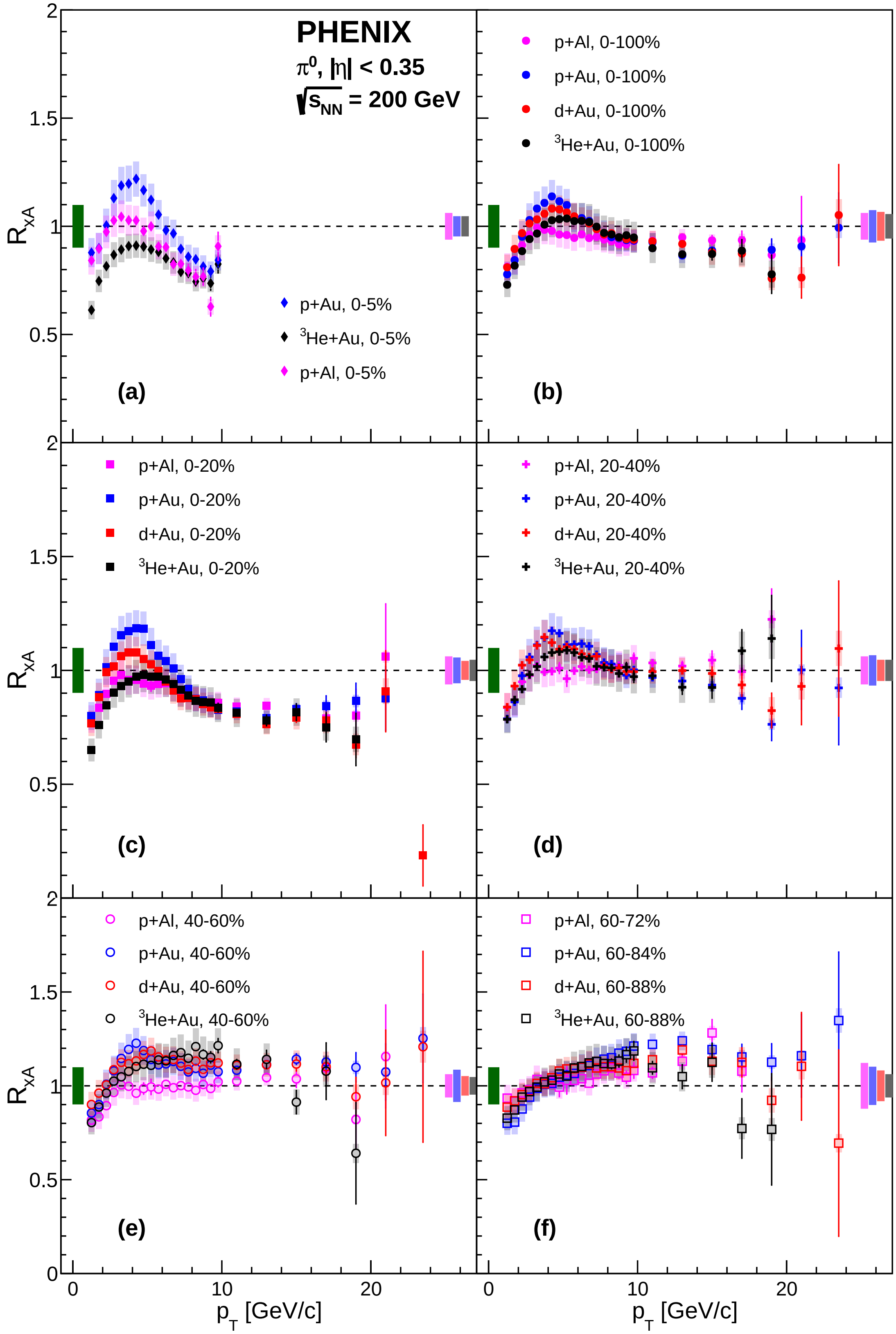

FIG. 7: Nuclear modification factors in p+Al, p+Au, d+Au, and ^{3}He+Au in five centrality bins and for inelastic collisions at $\sqrt{s_{NN}} = 200\,\mathrm{GeV}$. The error bars represent the statistical uncertainties, while the boxes represent the systematical uncertainties. The right boxes are the uncertainties of the $N_{\rm coll}$ collisions from the Glauber model, while the left box represents the overall normalization uncertainty from p+p collisions.

are two model independent conclusions that can be derived from the observations: (i) the underlying mechanism for the nuclear modification affects each projectile nucleus mostly independently, and (ii) the nuclear modification is not driven by the thickness of the nuclear matter traversed by the projectile.

Panel (a) in Fig. 8 shows $\langle R_{\mathrm{xA}} \rangle$ as function of N_{coll} for the lower p_{T} range from 4 to 6 GeV/c, covering the peak in R_{xA} for all systems. The $\langle R_{\mathrm{xA}} \rangle$ is remarkably close to binary scaling, with deviations that are visibly smaller than those observed at high p_{T} (see panel (b)). Another notable difference compared to the high p_{T} range is that all systems show similar deviations from binary scaling at the same N_{coll}. In contrast, the systems involving a Au target nucleus do not show a common trend with $N_{\mathrm{coll}}/N_{\mathrm{proj}}$ (panel c). These observations are qualitatively the same for any p_{T} window between 1 and 6 GeV/c. This suggests that the mechanism underlying the nuclear modification is different at high and low p_{T} with a transition in the 5 to 7 GeV/c range.

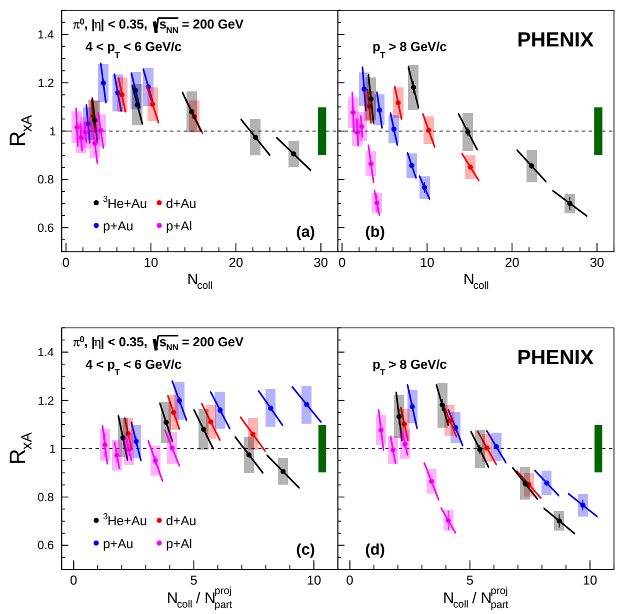

FIG. 8: Integrated R_{xA} in two different p_{T} regions versus the number of collisions per projectile participants. The left panel shows the region around the R_{xA} peak ($4 < p_{\mathrm{T}} < 6\,\mathrm{GeV}/c$) and the right panel shows the high p_{T} region ($p_{\mathrm{T}} > 8\,\mathrm{GeV}/c$). The statistical and systematic uncertainties are represented by error bars and boxes respectively around the data points. The tilted error bars represent the anti-correlated uncertainty on the y and x-axis due the N_{coll} calculations. The right bar around unity represents the overall normalization uncertainty from p+p collisions.

5. *Model Comparison and Discussion*

It is well known that the parton distribution function (PDF) of a nucleon is modified if the nucleon is within a nucleus [39]. The modifications increase with increasing number of nucleons in the nucleus. Like the PDFs themselves the nuclear parton distribution functions (nPDFs) are determined empirically by fitting a large variety of experimental data. Here three different nPDFs are considered: nNNPDFv1.0 [40], EPPS16 [41], and nCTEQ15 [42].

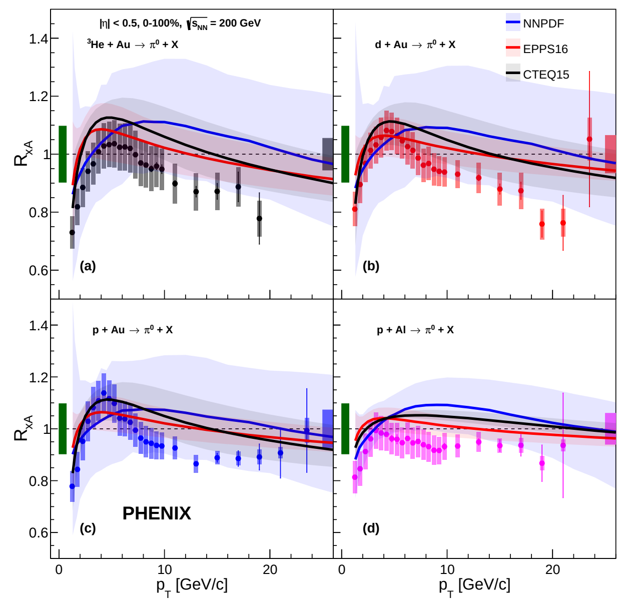

FIG. 9: R_{xA} for inelastic collisions compared to three different nuclear PDF calculations and their uncertainties. The data points include the statistical and systematical uncertainties. The left box around unity represents the overall normalization uncertainty on the p+p collisions and the right box represents the uncertainty from the calculated N_{coll}.

In Figure 9, the measured nuclear modification factors for inclusive p+Al, p+Au, d+Au, and ^{3}He+Au collisions are compared to the predictions using the three different nPDFs mentioned above. The central value of the predictions is represented by a line and the uncertainties from fitting the nPDF to data are given as shaded area. Due to their large uncertainties, all three nPDFs give R_{xA} predictions consistent with the data. However, looking at the central values, the predictions are in tension with the trends of the data. For example, for the nNNPDF case an enhancement is observed from 4 to above 20 GeV/c for all systems, with a maximum near 8 GeV/c, clearly not consistent with data. Looking at individual collision systems, EPPS16 and nCTEQ16 based calculations qualitatively, but not quantitatively, capture the general trends. The tension is most clearly visible when comparing the system size dependence. Each nPDF calculation predicts an ordering of the enhancement of R_{xA} in the peak region: ^{3}He+Au $>$ d+Au $>$ p+Au $>$ p+Al, which is significant as the systematic uncertainties on the nPDFs within one approach are highly correlated between systems. The ordering results from both the modification increasing with the target size and with the projectile size. In contrast, the data show the reverse ordering.

At high-p_T, the models predict an opposite, reverse ordering of the suppression of R_{xA}: ^{3}He+Au $<$ d+Au $<$ p+Au $<$ p+Al for the same reasons. In contrast, the data show a larger suppression, which is fairly independent of the collision system. However, given the systematic uncertainties on the R_{xA} scale, the nPDF predictions are consistent with the data at high p_T. The different trends, in particular at low p_T, of the nPDF calculations compared to the data suggest that there must be additional physics driving the nuclear modification beyond the nPDFs.

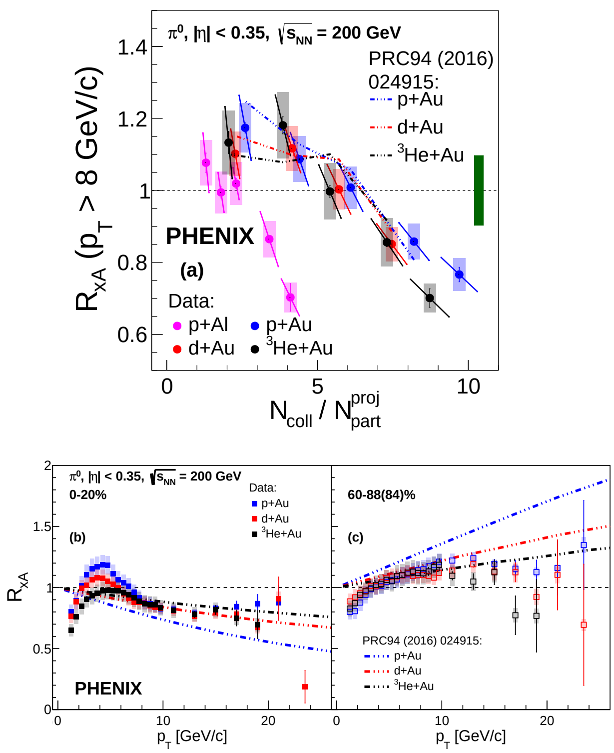

FIG. 10: The upper panel (a) shows the $\langle R_{xA}\rangle$ above $p_T = 8$ GeV/c as a function N_{coll}/N_{proj}. The data are compared to predictions from [43] for the consequences of high-x nucleon size fluctuations. The lower panels show the $\langle R_{xA}\rangle$ as a function of p_T for most central on left (b) and most peripheral on right panel (c) collisions.

The data show that at high p_T π^0 yields from small systems are suppressed relative to p+p in central event selections, while they are enhanced for peripheral selections. Furthermore, for p+Au, d+Au, and ^{3}He+Au, the $\langle R_{xA}\rangle$ values for $p_T > 8$ GeV/c are consistent with a superposition of independent collisions of the projectile nucleons. At the same time, p+Au and p+Al show nearly the same $\langle R_{xA}\rangle$ in the same centrality bin selection. These observations contradict any scenarios where parton energy loss would be responsible for the modification, which would necessarily result in an ordering of R_{xA} values as ^{3}He+Au $<$ d+Au $<$ p+Au $<$ p+Al ≤ 1 for the system dependence, with the suppression for each system being largest for central and $R_{xA} \sim 1$ for peripheral collisions.

Models that invoke nucleon size variations have been proposed to explain the suppression/enhancement pattern seen in the data [29, 30]. These models assume that nucleons with high-x partons have a more compact color configuration and thus will produce on average less binary collisions and target participants at the same impact parameter as nucleons without high-x partons. As a consequence, events with a high p_T π^0 would typically be biased towards smaller multiplicity of the overall event, leading to an apparent enhancement in peripheral event selections and a suppression in central events. The calculations from [43], which predicted jet R_{xA} for p+Au and ^{3}He+Au based on a comparison to d+Au data, are compared to π^0 $\langle R_{xA}\rangle$ above 8 GeV/c[1], see Figure 10 (a) panel. The observed centrality dependence is quite consistent with the data. It can be expected that in this model the same event selection bias would occur in p+Al collisions. It is important to note, however, that these models predict an ordering of R_{xA} with system size and centrality at higher p_T. For central collisions R_{xA} values follow ^{3}He+Au $<$ d+Au $<$ p+Au and for peripheral collisions the ordering is reversed. This is clearly seen in Figure 10 (b) and (c). In contrast, such an ordering is not supported by the data.

In [31], the bias of the event selection by centrality occurs because soft particle production away from the hard scattering process is suppressed, caused by the depletion of energy available in the projectile after the hard scattering process. R_{xA} calculated for d+Au with this model was consistent with preliminary d+Au data [31] and is also consistent with the final data within systematic uncertainties. It would be interesting to see these calculations expanded to the full variety of available data from small systems.

[1] Note that jet R_{xA} presented in [43] was converted to π^0 R_{xA} assuming $p_T(\pi^0) = 0.7 p_T{}^{jet} = 0.7 \times 100\text{GeV} \times x_p$ and $\langle R_{xA}\rangle \sim R_{xA}(p_T)$. This procedure was discussed with the authors.

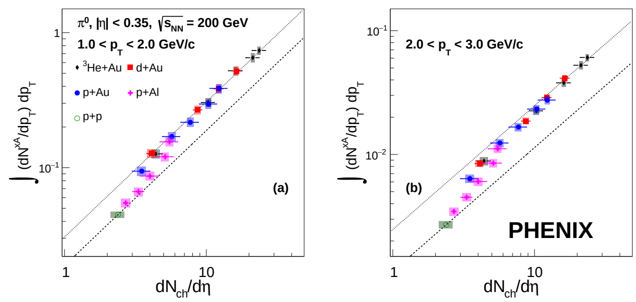

FIG. 11: Integrated yields for 1–2 GeV/c in panel (a) and 2–3 GeV/c in panel (b) as a function of charged particle multiplicity density at mid rapidity.

In recent years particle spectra from p+p collisions at the LHC have been interpreted in the context of hydrodynamic models and the presence of strong radial flow [44–47], but no predictions exist for small systems at RHIC energies that could be compared to the data. If the large anisotropies of particle production seen at RHIC in p+Au, d+Au, and ^{3}He+Au are indeed related to hydrodynamic expansion of the collision volume, as suggested in [24], then the same systems must also exhibit radial flow since the anisotropy would be a geometry driven modulation of radial flow. The effects of radial flow are typically most prominent at p_T below a few GeV/c, where soft particle production mechanisms dominate. In the presence of radial flow the π^0 yield would be shifted towards higher momentum by the velocity field. Accordingly, when comparing the shape of the π^0 momentum spectra from x+A to that from p+p, a depletion of the yield at the lowest p_T is expected, while at higher p_T the yield would be enhanced with a transition below 0.5 GeV/c. Since the p_T range of the π^0 data starts at 1 GeV/c, only the region where an enhancement would be expected can be studied here.

In order to look for possible indications of radial flow the integrated yields are calculated for two p_T ranges, 1–2 and 2–3 GeV/c, for all systems and event selections. The results are plotted in Figure 11 as function of the charged particle multiplicity density $dN_{ch}/d\eta$ at mid rapidity for the corresponding system and event selection. Also shown on each panel are two lines indicating integrated yields proportional to $dN_{ch}/d\eta$. The lower line is anchored to the p+p point following a trend of unchanged shape of the spectra, and the other one matches the yield for the 0–20% ^{3}He+Au selection. While the peripheral p+Al events follow the p+p trend, all other selections show higher integrated yields compared to the p+p trend. Above $dN_{ch}/d\eta \sim 10$ the data tends to be proportional to $dN_{ch}/d\eta$ again but at a much higher level.

The observed trend is qualitatively consistent with the presence of radial flow in small systems. Interestingly, the surprisingly rapid transition over the range from about 3 to 10 is similar to recent observations of low p_T direct photon emission [48], which also indicates a transition from p+p like emission to a significant enhancement of direct photons at similar event multiplicities. Furthermore, the presence of radial flow could naturally explain the much larger observed Cronin effect for protons from small systems [5], which so far has eluded a quantitative understanding. However, before drawing firm conclusions, more investigations are necessary. These should include the study of heavier hadrons, like Kaons and protons.

VII. SUMMARY

In summary, this paper presents new measurements of the invariant cross section of neutral pion production from p+p collisions and invariant yields from p+Al, p+Au, d+Au, and ^{3}He+Au at $\sqrt{s_{NN}} = 200\,\mathrm{GeV}$. For p+p the new results extend the measured range to $p_T \sim 25\,\mathrm{GeV}/c$ and improve statistical and systematic uncertainties compared to the previous measurement. NLO pQCD calculations are found to be consistent with the data as previously reported.

For p+Al, p+Au, d+Au, and ^{3}He+Au collisions at $\sqrt{s_{NN}} = 200\,\mathrm{GeV}$, π^0 p_T spectra from inelastic collisions and from centrality selected event samples were measured, including a sample of the 0–5% most central events for p+Al, p+Au, and ^{3}He+Au, which was recorded with a dedicated high multiplicity trigger.

At high transverse momentum ($p_T > 8$ GeV/c), where hard scattering processes are the dominant production mechanism, the nuclear modification factors for all collision systems are found to be nearly constant. For the same event selection in percent centrality, different collision systems exhibit the same constant value of R_{xA}. For the full inelastic cross section, R_{xA} is consistent with unity, pointing towards little or no nuclear modification of hard scatting processes in small systems. For the most central events, it is observed that R_{xA} is significantly below unity. However, R_{xA} increases monotonically with decreasing centrality and exceeds unity for peripheral collisions. For Au target nuclei, the $\langle R_{\mathrm{xA}} \rangle$ above p_T of 8 GeV/c shows a common trend with $N_{\mathrm{coll}}/N_{\mathrm{proj}}$. This indicates that, for hard scattering processes, the nucleons in the small projectile nucleus interact mostly independently with the Au target. For p+Al collisions, $\langle R_{\mathrm{xA}} \rangle$ does not follow the same trend. At the same event centrality, the p+Al $\langle R_{\mathrm{xA}} \rangle$ is the same as for p+Au, which suggests that whatever causes the change of R_{xA} with centrality does not depend on the target nucleus.

These observations disfavor scenarios where energy loss is a significant contributor to the nuclear modification of high p_T particle production in small systems. The counter-intuitive centrality dependence is likely linked to a mismatch of the centrality selection of events using charged particle multiplicity and mapping them to a number of binary collisions using the standard Glauber model. It seems that events with a high p_T π^0 are biased towards smaller underlying event multiplicity. This might be due to physical fluctuations of the proton size or simply due to energy conservation if high p_T jets are present.

For lower p_T, R_{xA} for all systems initially increases with p_T and reaches a peak near 4–6 GeV/c for central and semi-central collisions. For peripheral collisions, R_{xA} levels off to a constant at approximately the same high p_T value for all systems. For inelastic collisions and more central collisions, R_{xA} resembles what has been referred to as the Cronin effect in fixed target experiments - a rise, followed by a peak, followed by a plateau. However, unlike at lower energies, p+p and x+A π^0 cross sections are not related by a power $(AB)^{n(p_T)}$ with a common $n(p_T)$. Furthermore, the peak value around 4–6 GeV/c shows a clear system size dependence p+Au $>$ d+Au $>$ ^{3}He+Au $>$ p+Al, where the R_{xA} peak value is well above unity for p+Au and drops to close to unity for p+Al collisions.

While the shape of R_{xA} roughly resembles what is expected from the nuclear modification of PDFs, the observed system size dependence has exactly the reverse ordering of what was predicted by nPDF calculations. Therefore it is likely that nPDF's are insufficient to explain the nuclear modifications in small systems.

In the same p_T region, $\langle R_{xA}\rangle$ was used to study the dependence on centrality. For all systems, $\langle R_{xA}\rangle$ in the range 4–6 GeV/c follows a common trend with N_{coll}. At high p_T, $\langle R_{xA}\rangle$ scales with N_{coll}/N_{proj} for Au target nuclei. While at lower p_T, d+Au and ^{3}He+Au are not a superposition of p+Au like collisions. Consequently, very different mechanisms must contribute to the nuclear modification at high and low p_T. Radial flow is one possible mechanism to explain this trend, though further investigation is needed that is outside the scope of this paper.

Acknowledgments

Determined by runs for which new results are being released. For long papers, leave blank and Brant will add later.

[1] K. Adcox et al. (PHENIX), Phys. Rev. Lett. **88**, 022301 (2002), nucl-ex/0109003.
[2] S. S. Adler et al. (PHENIX), Phys. Rev. **C74**, 024904 (2006), nucl-ex/0603010.
[3] A. Adare et al. (PHENIX), Phys. Rev. Lett. **101**, 232301 (2008), 0801.4020.
[4] J. W. Cronin, H. J. Frisch, M. J. Shochet, J. P. Boymond, R. Mermod, P. A. Piroue, and R. L. Sumner, Phys. Rev. **D11**, 3105 (1975).
[5] D. Antreasyan, J. W. Cronin, H. J. Frisch, M. J. Shochet, L. Kluberg, P. A. Piroue, and R. L. Sumner, Phys. Rev. **D19**, 764 (1979).
[6] J. H. Kuhn, Phys. Rev. **D13**, 2948 (1976).
[7] M. Lev and B. Petersson, Z. Phys. **C21**, 155 (1983).
[8] X.-N. Wang, Phys. Rev. **C61**, 064910 (2000), nucl-th/9812021.
[9] Y. Zhang, G. I. Fai, G. Papp, G. G. Barnafoldi, and P. Levai, Phys. Rev. **C65**, 034903 (2002), hep-ph/0109233.
[10] B. Z. Kopeliovich, J. Nemchik, A. Schafer, and A. V. Tarasov, Phys. Rev. Lett. **88**, 232303 (2002), hep-ph/0201010.
[11] A. Accardi and D. Treleani, Phys. Rev. **D64**, 116004 (2001), hep-ph/0106306.
[12] I. Vitev and M. Gyulassy, Phys. Rev. Lett. **89**, 252301 (2002), hep-ph/0209161.
[13] D. Kharzeev, Y. V. Kovchegov, and K. Tuchin, Phys. Rev. **D68**, 094013 (2003), hep-ph/0307037.
[14] R. C. Hwa and C. B. Yang, Phys. Rev. Lett. **93**, 082302 (2004), nucl-th/0403001.
[15] V. Khachatryan et al. (CMS), JHEP **09**, 091 (2010), 1009.4122.
[16] B. Abelev et al. (ALICE), Phys. Lett. **B719**, 29 (2013), 1212.2001.
[17] G. Aad et al. (ATLAS), Phys. Rev. Lett. **110**, 182302 (2013), 1212.5198.
[18] S. Chatrchyan et al. (CMS), Phys. Lett. **B718**, 795 (2013), 1210.5482.
[19] A. Adare et al. (PHENIX), Phys. Rev. Lett. **111**, 212301 (2013), 1303.1794.
[20] A. Adare et al. (PHENIX), Phys. Rev. Lett. **115**, 142301 (2015), 1507.06273.
[21] C. Aidala et al., Phys. Rev. **C95**, 034910 (2017), 1609.02894.
[22] C. Aidala et al. (PHENIX), Phys. Rev. Lett. **120**, 062302 (2018), 1707.06108.
[23] A. Adare et al. (PHENIX), Phys. Rev. C **97**, 064904 (2018), 1710.09736.
[24] C. Aidala et al. (PHENIX), Nature Phys. **15**, 214 (2019), 1805.02973.
[25] A. Adare et al. (PHENIX), Phys. Rev. **C90**, 034902 (2014), 1310.4793.
[26] G. Aad et al. (ATLAS), Phys. Lett. **B748**, 392 (2015), 1412.4092.
[27] A. Adare et al. (PHENIX), Phys. Rev. Lett. **116**, 122301 (2016), 1509.04657.
[28] Z.-B. Kang, I. Vitev, and H. Xing, Phys. Rev. **C92**, 054911 (2015), 1507.05987.
[29] M. Alvioli, B. A. Cole, L. Frankfurt, D. V. Perepelitsa, and M. Strikman, Phys. Rev. **C93**, 011902 (2016), 1409.7381.
[30] M. Alvioli, L. Frankfurt, D. Perepelitsa, and M. Strikman, Phys. Rev. **D98**, 071502 (2018), 1709.04993.
[31] M. Kordell and A. Majumder, Phys. Rev. C **97**, 054904 (2018), 1601.02595.
[32] A. Adare et al. (PHENIX), Phys. Rev. **D76**, 051106 (2007), 0704.3599.
[33] L. Aphecetche et al. (PHENIX), Nucl. Instrum. Meth. **A499**, 521 (2003).
[34] S. Adler et al. (PHENIX), Phys. Rev. C **76**, 034904 (2007), nucl-ex/0611007.
[35] B. Alver, M. Baker, C. Loizides, and P. Steinberg (2008),

0805.4411.
[36] A. Valassi, Nucl. Instrum. Meth. **A500**, 391 (2003).
[37] B. Jager, A. Schafer, M. Stratmann, and W. Vogelsang, Phys. Rev. **D67**, 054005 (2003), hep-ph/0211007.
[38] P. B. Straub et al., Phys. Rev. Lett. **68**, 452 (1992).
[39] M. Arneodo, Phys. Rept. **240**, 301 (1994).
[40] R. Abdul Khalek, J. J. Ethier, and J. Rojo (NNPDF), Eur. Phys. J. C **79**, 471 (2019), 1904.00018.
[41] K. J. Eskola, P. Paakkinen, H. Paukkunen, and C. A. Salgado, Eur. Phys. J. C **77**, 163 (2017), 1612.05741.
[42] K. Kovarik et al., Phys. Rev. D **93**, 085037 (2016), 1509.00792.
[43] D. McGlinchey, J. Nagle, and D. Perepelitsa, Phys. Rev. C **94**, 024915 (2016), 1603.06607.
[44] T. Bhattacharyya, J. Cleymans, A. Khuntia, P. Pareek, and R. Sahoo, Eur. Phys. J. A **52**, 30 (2016), 1507.08434.
[45] D. Sarkar, S. Choudhury, and S. Chattopadhyay, Phys. Lett. B **760**, 763 (2016).
[46] Y. Hirono and E. Shuryak, EPJ Web Conf. **141**, 01008 (2017).
[47] A. Khuntia, H. Sharma, S. Kumar Tiwari, R. Sahoo, and J. Cleymans, Eur. Phys. J. A **55**, 3 (2019), 1808.02383.
[48] A. Adare et al. (PHENIX), Phys. Rev. Lett. **123**, 022301 (2019), 1805.04084.

APPENDIX